Fluctuations of the Atlantic North Equatorial Undercurrent and associated changes in oxygen transports

Kristin Burmeister[1], Joke F Luebbecke[1], Peter Brandt[2], Martin Claus[2], and Johannes Hahn[2]

[1]GEOMAR
[2]GEOMAR Helmholtz Centre for Ocean Research Kiel

November 21, 2022

Abstract

Although the core velocity of the Atlantic North Equatorial Undercurrent (NEUC) is low (0.1-0.3ms) it has been suggested to act as an important oxygen supply route towards the oxygen minimum zone in the eastern tropical North Atlantic. For the first time the intraseasonal to interannual NEUC variability and its impact on oxygen is investigated based on shipboard and moored velocity observations around 5°N, 23°W. In contrast to previous studies that were mainly based on models or hydrographic data, we find hardly any seasonal cycle of NEUC transports in the central Atlantic. The NEUC transport variability is instead dominated by sporadic intraseasonal events. Only some of these events are associated with high oxygen levels suggesting an occasional eastward oxygen supply by NEUC transport events. Nevertheless, they likely contribute to the local oxygen maximum in the mean shipboard section along 23°W at the NEUC core position.

Fluctuations of the Atlantic North Equatorial Undercurrent and associated changes in oxygen transports

K. Burmeister[1], J. F. Lübbecke[2,3], P. Brandt[2,3], M. Claus[2,3], and J. Hahn[2]

[1]SAMS, Scottish Marine Institute, Oban, Argyll, PA37 1QA, United Kingdom
[2]GEOMAR Helmholtz Centre for Ocean Research Kiel, Düsternbrooker Weg 20, 24105 Kiel, Germany
[3]Christian-Albrechts-Universität zu Kiel, Christian-Albrechts-Platz 4, 24118 Kiel, Germany

Key Points:

- Transport time series of the Atlantic North Equatorial Undercurrent estimated from moored observations
- North Equatorial Undercurrent dominated by intraseasonal variability, only weak seasonal cycle
- Occasional increase of eastward oxygen supply by North Equatorial Undercurrent due to short sporadic events

Corresponding author: Kristin Burmeister, `kburmeister@geomar.de`

Abstract

Although the core velocity of the Atlantic North Equatorial Undercurrent (NEUC) is low ($0.1 - 0.3\,\mathrm{m\,s^{-1}}$) it has been suggested to act as an important oxygen supply route towards the oxygen minimum zone in the eastern tropical North Atlantic. For the first time the intraseasonal to interannual NEUC variability and its impact on oxygen is investigated based on shipboard and moored velocity observations around 5°N, 23°W. In contrast to previous studies that were mainly based on models or hydrographic data, we find hardly any seasonal cycle of NEUC transports in the central Atlantic. The NEUC transport variability is instead dominated by sporadic intraseasonal events. Only some of these events are associated with high oxygen levels suggesting an occasional eastward oxygen supply by NEUC transport events. Nevertheless, they likely contribute to the local oxygen maximum in the mean shipboard section along 23°W at the NEUC core position.

Plain Language Summary

In the eastern tropical North Atlantic a zone of low-oxygen waters exists between 100 m and 700 m depth due to high oxygen consumption and weak exchange of water masses. Long-term oxygen changes in this zone have been reported with possible impacts on, for example, the ecosystem or the available habitat for fish. Typically, water masses in that region are exchanged via weak eastward and westward currents. As the oxygen concentration in the western Atlantic basin is high, an eastward current such as the North Equatorial Undercurrent (NEUC) may transport oxygen-rich waters into the eastern low-oxygen zone. Given the east-west difference in oxygen concentration, we assume that a stronger NEUC is transporting more oxygen-rich water from the western towards the eastern basin. This is the first study that investigates the variations in NEUC transport based on direct velocity measurements at 5°N, 23°W. In contrast to previous studies based on model simulations or hydrographic data, we do not find a seasonal cycle of the NEUC transport. Instead, changes of the NEUC transport are dominated by bursts of eastward flow which persist for a few months. These eastward flow bursts are only occasionally associated with higher oxygen concentrations.

1 Introduction

The circulation of the upper tropical Atlantic Ocean is characterized by a complex current system which takes part in the wind-driven equatorial gyre circulation, the shallow subtropical and tropical overturning cells and the basin-wide Atlantic meridional overturning circulation (e.g. Hazeleger & Drijfhout, 2006; Schott et al., 2004). Zonal currents play a key role in the basin wide distribution of water mass properties and affect the transport of heat, salt and biogeochemical components such as oxygen (e.g. Brandt et al., 2015; Hazeleger & Drijfhout, 2006; Schott et al., 2004). The North Equatorial Undercurrent (NEUC) is an eastward flowing subsurface (here defined in the depth range 65-270 m) current centered at 5°N. Its upper limit is commonly defined as the $24.5\,\mathrm{kg\,m^{-3}}$ neutral density layer, which separates the tropical surface water from the subtropical underwater (e.g. Bourlès et al. , 1999; Goes et al., 2013; Schott et al., 1995). Although the NEUC core velocity ($0.1\,\mathrm{m\,s^{-1}}$ to $0.3\,\mathrm{m\,s^{-1}}$) is one of the lowest among the wind-driven off-equatorial currents in the tropical Atlantic the NEUC has been suggested to act as an important oxygen supply route towards the oxygen minimum zone in the eastern tropical North Atlantic (Brandt et al., 2010; Stramma et al., 2008).

Model studies generally agree that the NEUC is mainly in geostrophic balance but its driving mechanism is under discussion. Potential mechanisms that were described for the NEUC or similar subsurface currents in other tropical basins are the conservation of angular momentum of the tropical overturning cells (Marin et al., 2000), the Eliassen-Palm flux associated with the propagation of Tropical Instability Waves (TIWs; Jochum & Malanotte-Rizzoli, 2004) or the pull of upwelling within domes in the eastern basin or at the eastern boundary (Furue et al., 2007, 2009; McCreary et al., 2002).

Until now, the seasonal to long-term variability of the NEUC has been investigated based on model output (Burmeister et al., 2019; Hüttl-Kabus & Böning, 2008) or geostrophic velocities derived from a combination of hydrography and satellite data (Goes et al., 2013). In these studies, a seasonal cycle of the NEUC with amplitudes of 1 Sv to 3.5 Sv was identified. In general, NEUC transport estimates derived from meridional ship sections are obscured by mesoscale activity (Weisberg & Weingartner, 1988) and interannual variability (Hüttl-Kabus & Böning, 2008). So far, studies based on shipboard velocity observations have not been able to detect a seasonal cycle of the NEUC (Bourlès et al., 2002, 1999; Burmeister et al., 2019; Schott et al., 2003, 1995; Urbano et al., 2008).

For the first time, we will investigate the NEUC variability using direct velocity observations. In this study we reconstruct the eastward transport associated with the NEUC at 5°N, 23°W using moored velocity observations from June 2006 to February 2008 and November 2009 to January 2018 in combination with 24 meridional ship sections taken between 21°W and 26°W. This study aims to investigate the intraseasonal to interannual variability of the NEUC and its impact on oxygen levels.

2 Data

Moored Acoustic Doppler Current Profiler (ADCP) velocity, hydrography and oxygen data are available at 5°N, 23°W (Jun 2006-Feb 2008, Nov 2009-Jan 2018) as well as at 4.6°N, 22.4°W and 4.5°N, 23.4°W (Nov 2012-Apr 2014). All instruments were set to a sampling rate of 2 h or higher. The upper limit of the ADCP observations varies between 65 m and 85 m, the lower limit is at least 755 m. The moored velocity data were linearly interpolated onto a regular time-depth grid (12 h ×10 m), and a 40-day low-pass Butterworth filter was applied to remove tides from the time series. As the NEUC is located approximately between 3.5°N and 6°N and in a depth of about 65 m to 270 m at 23°W (Burmeister et al., 2019) the moored velocity observations do not always cover the entire extent of the NEUC which can result in an underestimation of its mean transport. Observations of dissolved oxygen, temperature, conductivity and pressure were used from respective sensors that were installed at the mooring at 5°N, 23°W in 100 m, 200 m, and 300 m depth. The moored hydrography and oxygen data were interpolated onto a 12-h time grid. This data set is an extension of the one used in Hahn et al. (2014, see Text S1 for more details).

In addition to the mooring time series we use data from 24 meridional ship sections taken between 21°W and 26°W in the time period 2002 to 2018 (Table S1). Only shipboard ADCP, hydrography and oxygen sections that cover at least the upper 350 m between 0° and 10°N are used. The ship sections are an extension of the data set used in Burmeister et al. (2019, see Text S1 for more details).

3 Observed velocity variability at 5°N, 23°W

Moored ADCP measurements at 5°N, 23°W show a weak mean eastward velocity with maximum values of $9\,\mathrm{cm\,s^{-1}}$ at the upper limit of the ADCP range (85 m), while the meridional velocity varies around zero (Fig. 1 a and b). In the upper 300 m zonal and meridional velocities exhibit anomalies of comparable magnitude. The periodogram of the horizontal velocity components indicates variability over a range of frequencies, in particular in the intraseasonal band (Fig. 1 c). While the zonal velocity exhibits variability mainly for periods greater than 70 days, the meridional velocity is dominated by variability with periods between 35 and 75 days which is associated with TIWs (Jochum & Malanotte-Rizzoli, 2003). The zonal velocity, while eastward in the mean, occasionally changes to westward. Its variability is characterized by strong eastward anomalies with a duration of about one to five months occurring without a clear seasonal preference. Unexpectedly, the seasonal cycle of the zonal velocity is much weaker than found in previous studies (Burmeister et al., 2019; Goes et al., 2013; Hüttl-Kabus & Böning, 2008). The annual harmonic fit with a maximum amplitude of 3 $\mathrm{cm\,s^{-1}}$ only explains between 2% (85 m) and 9% (300 m) of the zonal velocity variability. For the semi-annual harmonic we derived a maximum amplitude of 5 $\mathrm{cm\,s^{-1}}$ and an explained variance between 11% (75 m) and 1% (300 m).

4 NEUC transport estimates at 23°W

In this study, the NEUC transport was estimated by four different methods using only eastward velocities. (i) We calculated the NEUC transport between the 24.5 $\mathrm{kg\,m^{-3}}$ and 26.8 $\mathrm{kg\,m^{-3}}$ neutral density surfaces from 24 ship sections using a path following algorithm developed by Hsin and Qiu (2012) (Fig. 2, green diamonds). This method follows the current core, thereby avoiding artifacts in the transport calculation if the current is meridionally migrating (see Text S2 for more details). Using this method we estimate a mean NEUC transport of 2.7±0.4 Sv. Uncertainties are given in terms of the standard error. In the following, we consider this estimate as a reference NEUC transport keeping in mind that the NEUC transport estimate from ship sections can be obscured by mesoscale activity (Weisberg & Weingartner, 1988) and interannual variability (Hüttl-Kabus & Böning, 2008).

(ii) The second approach is also based on ship sections only, but with a fixed smaller integration box to be consistent with NEUC transports calculated from a combination of ship mounted and moored observations. We integrate the meridional sections of zonal velocity between 4.25°N and 5.25°N, 65 m and 270 m (Fig. 2, black circles). The mean fixed box integrated transport derived from ship sections is 1.4±0.2 Sv. The fixed box integrated method underestimates the NEUC strength by 1.3 Sv. However, it represents the variability of the reference NEUC transport well (R=0.91, Fig. S2a).

(iii) We reconstruct the NEUC transport combining moored velocity observations at 5°N, 23°W as well as 4.6°N, 22.4°W and 4.5°N, 23.4°W and ship sections following the optimal width (OW) method described in Brandt et al. (2014). This method aims to find an optimal latitude range W_i for each mooring position i to reconstruct the latitudinally integrated zonal velocity $U(z,t)$ by:

$$U(z,t) = \sum_{i=1}^{3} W_i u_i(z,t) \tag{1}$$

For this purpose, we latitudinally integrate the eastward velocities of each ship section from 4.25°N to 5.25°N. The latitudinally integrated velocity is then regressed onto the eastward velocities of the ship sections at the three mooring position between 65 m and 270 m depth to obtain W_i. We estimated that the moorings at 5°N, 4.6°N and 4.5°N correspond to latitude ranges, W_i, of 0.46°, 0.18° and 0.37°, respectively. The NEUC transport is then reconstructed by integrating Equation 1 over the same depth range as for method (ii) (Fig. 2, blue line). Note that data from all three mooring positions are only available for the time period November 2012 to April 2014. The root mean square error of the reconstructed transport using method (iii) and the box integrated transport (method ii) using the shipboard data is 0.16 Sv. The mean reconstructed transport is 0.9±0.3 Sv. For a validation of the method see Text S2 in the supplementary information.

(iv) This method is similar to method (iii) but uses moored velocity observations only at 5°N, 23°W to obtain a longer transport time series (Fig. 2 grey line). Here, the 5°N mooring corresponds to a latitude range of 0.88°. Although the root mean square error between the reconstructed transport and the box integrated transport increases (0.51 Sv) when using only one mooring, the reconstructed transport based on one mooring agrees well with the one reconstructed using three moorings (R=0.89). The mean NEUC transport is the same as estimated for method (iii), i.e. 0.9±0.2 Sv.

In the following we will analyze the NEUC variability based on the reconstructed time series using only the mooring at 5°N, 23°W. Although the reconstructed transport time series from moored velocity observations tends to underestimate the mean current strength of the NEUC, we still consider the variability to be captured to a large extent. This is supported by transport estimates based on all three moorings combined with zonal velocity sections between 3.5°N and 6.0°N which agree reasonably well with the transport time series reconstructed by method (iii) accounting for velocities between 4.25°N and 5.25°N only (Fig. S2-S5, Text S2).

5 NEUC variability

Similar to the zonal velocity, the NEUC transport is dominated by strong eastward anomalies that persist between one and five months. The transport time series do not exhibit a seasonal cycle. The explained variance of the annual and semi-annual harmonic is only 2% and 3%, respectively. We therefore focus the analysis on the intraseasonal eastward flow events. Rather arbitrary, we define a strong eastward flow event if the NEUC transport exceed 2.5 times the standard deviation of the complete monthly mean time series. We find eight such events which take about one to five months to develop, peak and fade away (duration from local minimum to minimum in the transport time series). They have a maximum monthly mean transport between 2.3 Sv and 3.8 Sv and peak without a clear seasonal preference (3 in January, 1 each in April, May, June, August and December). During these events the 12-hourly transports reach maximum values from 3.8 Sv to 7.2 Sv.

The NEUC at 5°N, 23°W appears to be rather weak and it is likely that there are different generation mechanisms for the strong eastward flow events. The short period of intraseasonal events implies that the upwelling within the Guinea Dome in the eastern basin as suggested by McCreary et al. (2002) and Furue et al. (2007, 2009) may not be of first order in forcing them. To investigate the role of the wind forcing for the strong eastward flow events we linearly regressed zonal wind stress anomalies (Bentamy & Fillon, 2012; Kobayashi et al., 2015; Large & Yeager, 2004) onto the NEUC transport time series (Fig. S6, Text S3). Easterly wind stress anomalies in the eastern equatorial basin are leading the NEUC transports by one to two months. We hypothesize that these zonal wind stress anomalies may force equatorial Kelvin waves reflecting at the eastern boundary into westward propagating Rossby waves and poleward propagating coastal trapped waves. The northward propagating waves may shed Rossby waves when arriving at the exit of the Gulf of Guinea where the coastline turns northward. Such remotely forced Rossby waves may reach 5°N, 23°W, causing the observed eastward flow events. Rossby waves at 5°N, 23°W can also be forced locally by wind stress curl anomalies of small meridional scale (Burmeister et al., 2016; Foltz et al., 2010) or remotely generated by the radiation of Rossby waves from coastal trapped waves generated by local wind anomalies in the Gulf of Guinea (Chu et al., 2007). However, in a composite analysis of sea level anomalies we could not clearly identify a reflection of an equatorial Kelvin wave at the eastern boundary or a Rossby wave propagating from the eastern basin to 5°N, 23°W prior to any eastward flow event.

6 NEUC and oxygen

The NEUC is thought to transport oxygen rich water from the western boundary towards the generally poorly ventilated eastern tropical North Atlantic (Brandt et al., 2010; Stramma et al., 2008). The mean ship section indicates a local oxygen maximum which is associated with the NEUC and single ship sections often show maxima in the area of the NEUC (Fig. 3). Here we will investigate if the strong eastward NEUC events are associated with an increased eastward oxygen transport using moored observations.

We calculated oxygen anomalies on isopycnals. First, a temporal mean oxygen profile as a function of density was calculated from the mooring time series. Next, for each time step, the oxygen anomaly was calculated with respect to the mean oxygen value of the respective density. Finally we applied a second-order 30-day low-pass Butterworth filter to both, the transport and oxygen time series (Fig. 3).

In 100 m and 200 m depth, we found a significant positive correlation between the NEUC transport and oxygen anomalies ($R_{\mathrm{max,100m}} = 0.35$, NEUC leads by 16 days; $R_{\mathrm{max,200m}} = 0.35$, NEUC leads by 2.5 days), while in 300 m depth, which is just below the NEUC, the correlation is not significant ($R_{300m} = 0.05$, zero lag). If data is available, positive oxygen anomalies can be found during most of the strong eastward flow events except for in 100 m depth during the 2012 and 2014 event. 2017 seems to be an exceptional year in the moored time series with the two strongest eastward flow events occurring consecutively within six months. Additionally, these two events are associated with some of the highest oxygen anomalies observed. The correlation between oxygen and NEUC transport anomalies during these two events is much higher compared to the rest of the time series. The correlation between the time series for the period from September 2016 to February 2018 is 0.63 (NEUC leads by 13.5 days) and 0.56 (NEUC leads by 1.5 days) in 100 m and 200 m depth, respectively.

Positive oxygen anomalies also occur independently from strong eastward flow events and may be associated with changes in the meridional velocity. On intraseasonal time scales, zonal and meridional velocity anomalies are of similar strength and the dominant frequency band of the meridional velocity (30 to 70 days) overlaps with the frequency of the strong eastward flow events (one to five months). It is thus not possible to clearly differentiate between the effect of meridional and zonal velocity on oxygen values at the mooring position. Yet, we find no significant correlation between the 30-day low-pass filtered meridional velocity and oxygen anomalies ($-0.12 \leq R \leq 0.06$ at zero lag) (Fig. S7).

7 Summary and Discussion

The NEUC is an eastward flowing current centered around 5°N in the tropical Atlantic. Although its core velocity is weak (below $0.3\,\mathrm{m\,s^{-1}}$) it is thought to act as an important oxygen supply route towards the eastern tropical North Atlantic oxygen minimum zone (Brandt et al., 2010; Stramma et al., 2008). For the first time we reconstructed a time series of the NEUC transport based purely on direct velocity observations. By combining moored zonal velocities at 5°N, 23°W and meridional ship sections along ~23°W we obtained a NEUC transport time series from June 2006 to February 2008 and November 2009 to January 2018. In contrast to previous studies (Burmeister et al., 2019; Goes et al., 2013; Hüttl-Kabus & Böning, 2008), neither the moored zonal velocity at 5°N (Fig. 1) nor the reconstructed eastward NEUC transport (Fig. 2) exhibits a pronounced seasonal cycle. We find that both time series are dominated by strong intraseasonal eastward flow events which can peak throughout the year (Fig. 1 and 2). Although in the mean meridional ship sections the zonal velocity maximum associated with the NEUC coincides with a local oxygen maximum, we find that the eastward flow events are only occasionally associated with high oxygen levels (Fig. 3).

We reconstructed the NEUC transport at 23°W based on velocity observations from three moorings and 24 meridional ship sections (Fig. 2). To obtain a longer time series we then reconstructed the NEUC variability based on data from only one mooring position. The comparison with the three-mooring solution indicates that the variability is dominated by a meridionally homogeneous structure covering the complete integration box (Fig. S3). However, the method has some limitations. The used integration box does not cover the entire NEUC region (Fig. S1). Consequently, our method is underestimating the true NEUC transport. A comparison of the box integrated transport calculated from ship sections with a reference transport calculated from ship sections using a path following algorithm indicates that the box integrated transport represents the variability of the NEUC reasonably well (R=0.9, Fig. S2 and S5). An additional uncertainty of the reconstructed transport is due to the upper range of the moored velocity observations that varies between 65 m and

85 m, i.e. the moored observations do not always cover the entire NEUC depth range. In summary, the used method is underestimating the true NEUC strength but it is still capable of representing its variability, as this is dominated by a homogeneous structure in latitude and depth.

Within the scope of this paper we could not identify a clear forcing mechanism for the strong eastward flow events. We found that easterly wind stress anomalies in the eastern equatorial basin are leading the NEUC transport by one to two months. Zonal wind stress anomalies and associated wind stress curl anomalies could directly (Burmeister et al., 2016; Foltz et al., 2010) or remotely (Chu et al., 2007) force Rossby waves which reach 5°N, 23°W to cause the observed eastward flow events. However, we could not clearly identify a Rossby wave propagating from the eastern basin to 5°N, 23°W prior to any event. Other potential mechanisms might include nonlinear processes resulting e.g. in the development of multiple cores that were discussed by Furue et al. (2007). These cores that were superimposed on the otherwise linear arrested front dynamics (Dewar et al., 1991) were identified in simulations with enhanced horizontal resolution.

Finally, we investigated the relationship between the NEUC transport events and oxygen. In 2017, eastward transport and oxygen anomalies agree very well. For other events the correlation is weaker or non-existent (Fig. 3). One possible explanation is that the local oxygen maximum associated with the NEUC is not located directly at 5°N as visible in the meridional ship sections of March 2017 (Fig. 3b,e). In that case the higher oxygen concentrations are simply not captured by the mooring. Another explanation may be that some strong eastward flow events are not connected to the well-ventilated western boundary, but are instead supplied out of the westward flow of low-oxgen waters north and south of the NEUC. For example, in the meridional section of February 2018, we find strong eastward velocities between 4°N and 5°N at 50 m and 100 m depth that are associated with low oxygen concentrations, which might be due to a recirculation of low-oxygen waters typically present south of the NEUC (Fig. 3c and f; Burmeister et al., 2019). As the zonal velocity events with a duration between one and five months overlap with the dominant frequency band of meridional velocity (30 to 70 days) it is not possible to clearly differentiate between the effect of meridional and zonal velocity on oxygen. However, we did not find any correlation between the meridional velocity and oxygen anomalies on intraseasonal time scales at 5°N, 23°W. Furthermore, Hahn et al. (2014) found that the mean meridional eddy flux at the mooring position is not significantly different from zero. Consistent with previous studies

(Burmeister et al., 2019; Hahn et al., 2014; Weisberg & Weingartner, 1988), we suggest that a continuous flow of oxygen-rich water from the western boundary toward the eastern Atlantic basin by the NEUC is regularly altered by TIWs or other mesoscale recirculations. This can explain why not all NEUC transport events are associated with higher oxygen levels. Nevertheless, the significant positive correlation between the 30-day low-pass filtered NEUC transport and oxygen anomalies at 5°N, 23°N (Fig. 3) indicates that the NEUC transport events likely result in an elevated mean eastward oxygen transport and presumably contribute to sustain the oxygen maximum observed in ship sections at the NEUC core position.

Acknowledgments

This study was funded by the Deutsche Forschungsgemeinschaft as part of the Sonderforschungsbereich 754 "Climate-Biogeochemistry Interactions in the Tropical Ocean," through several research cruises with RV L'Atalante, RV Maria S. Merian, RV Meteor, and RV Polarstern, by the project FOR1740 and by the Deutsche Bundesministerium für Bildung und Forschung (BMBF) as part of projects RACE (03F0651B) and RACE-Synthesis (03F0824C). We thank the captains, crews, scientists, and technical groups involved in the different national and international research cruises to the eastern tropical North Atlantic that contributed to collecting CTD, velocity as well as mooring data, and making them freely available. We thank Rebecca Hummels for post-processing of the recent mooring and ship section data. The shipboard data are accessible at `https://doi.pangaea.de/10.1594/PANGAEA.899052`. The mooring data are accessible at `https://doi.pangaea.de/10.1594/PANGAEA.903913`. We are grateful to NOAA/PMEL and NOAA/AOML for making the data of the PIRATA Northeast Extension cruises freely available at `https://www.aoml.noaa.gov/phod/pne/cruises.php`. ASCAT data were obtained from the Centre de Recherche et d'Exploitation Satellitaire (CERSAT), at IFREMER, Plouzané (France) and are available at `ftp://ftp.ifremer.fr/ifremer/cersat/products/gridded/MWF/L3/ASCAT/Daily/`. Global Ocean Gridded L4 sea surface heights and derived variables were made available by E.U. Copernicus Marine Environment Monitoring Service (CMEMS). The data is available at `http://marine.copernicus.eu/services-portfolio/access-to-products/?option=com_csw&view=details&product_id=SEALEVEL_GLO_PHY_L4_REP_OBSERVATIONS_008_047`. The JRA-55 reanalysis surface winds used for this study are provided by the Japanese 55-year Reanalysis (JRA-55) project carried out by the Japan Meteorological Agency (JMA) and

is available at `https://jra.kishou.go.jp/JRA-55/index_en.html#jra-55` after registration.

References

Bentamy, A., & Fillon, D. C. (2012). Gridded surface wind fields from Metop/ASCAT measurements. *Int. J. Remote Sens.*, *33*(6), 1729–1754. doi: 10.1080/01431161.2011.600348

Bourlès, B., D'Orgeville, M., Eldin, G., Gouriou, Y., Chuchla, R., DuPenhoat, Y., & Arnault, S. (2002). On the evolution of the thermocline and subthermocline eastward currents in the Equatorial Atlantic. *Geophys. Res. Lett.*, *29*(16), 32–1–32–4. doi: 10.1029/2002GL015098

Bourlès, B., Gouriou, Y., & Chuchla, R. (1999). On the circulation in the upper layer of the western equatorial Atlantic. *J. Geophys. Res. Ocean.*, *104*(C9), 21151–21170. doi: 10.1029/1999JC900058

Brandt, P., Bange, H. W., Banyte, D., Dengler, M., Didwischus, S.-H., Fischer, T., Greatbatch, R. J., Hahn, J., Kanzow, T., Karstensen, J., Körtzinger, A., Krahmann, G., Schmidtko, S., Stramma, L., Tanhua, T., & Visbeck, M. (2015). On the role of circulation and mixing in the ventilation of oxygen minimum zones with a focus on the eastern tropical North Atlantic. *Biogeosciences*, *12*(2), 489–512. doi: 10.5194/bg-12-489-2015

Brandt, P., Funk, A., Tantet, A., Johns, W. E., & Fischer, J. (2014). The Equatorial Undercurrent in the central Atlantic and its relation to tropical Atlantic variability. *Clim. Dyn.*, *43*(11), 2985–2997. doi: 10.1007/s00382-014-2061-4

Brandt, P., Hormann, V., Körtzinger, A., Visbeck, M., Krahmann, G., Stramma, L., ... Schmid, C. (2010). Changes in the Ventilation of the Oxygen Minimum Zone of the Tropical North Atlantic. *J. Phys. Oceanogr.*, *40*(8), 1784–1801. doi: 10.1175/2010JPO4301.1

Burmeister, K., Lübbecke, J. F., & Brandt, P. (2016). Revisiting the cause of the eastern equatorial Atlantic cold event in 2009. *J. Geophys. Res. Ocean.*, *7*(121), 4777–4789. doi: 10.1002/2016JC011719

Burmeister, K., Lübbecke, J. F., Brandt, P., & Duteil, O. (2019). Interannual variability of the Atlantic North Equatorial Undercurrent and its impact on oxygen. *J. Geophys. Res. Ocean.*, *124*(4), 2348-2373. doi: 10.1029/2018JC014760

Chu, P. C., Ivanov, L. M., Melnichenko, O. V., & Wells, N. C. (2007). On long baroclinic Rossby waves in the tropical North Atlantic observed from profiling floats. *J. Geophys. Res.*, *112*(C5), C05032. doi: 10.1029/2006JC003698

Dewar, W. K. (1991). Arrested fronts. *J. Mar. Res.*, *49*, 21–52. doi: 10.1357/002224091784968576

Fischer, J., Brandt, P., Dengler, M., Müller, M., & Symonds, D. (2003). Surveying the upper ocean with the ocean surveyor: A new phased array Doppler current profiler. *J. Atmos. Ocean. Technol.*, *20*(5), 742–751. doi: 10.1175/1520-0426(2003)20⟨742:STUOWT⟩2.0.CO;2

Foltz, G. R., & McPhaden, M. J. (2010). Interaction between the Atlantic meridional and Niño modes. *J. Geophys. Res.*, *37*(18), L18604. doi: 10.1029/2010GL044001

Furue, R., McCreary Jr., J. P., Yu, Z., & Wang, D. (2007). Dynamics of the Southern Tsuchiya Jet*. *J. Phys. Ocean.*, *37*(3), 531–553. doi: 10.1175/JPO3024.1

Furue, R., McCreary Jr., J. P., & Yu, Z. (2009). Dynamics of the Northern Tsuchiya Jet*. *J. Phys. Oceanogr.*, *39*(9), 2024–2051. doi: 10.1175/2009JPO4065.1

Goes, M., Goni, G., Hormann, V., & Perez, R. C. (2013). Variability of the Atlantic off-equatorial eastward currents during 1993-2010 using a synthetic method. *J. Geophys. Res. Ocean.*, *118*(6), 3026–3045. doi: 10.1002/jgrc.20186

Hahn, J., Brandt, P., Greatbatch, R. J., Krahmann, G., & Körtzinger, A. (2014). Oxygen variance and meridional oxygen supply in the Tropical North East Atlantic oxygen minimum zone. *Clim. Dyn.*, *43*(11), 2999–3024. doi: 10.1007/s00382-014-2065-0

Hahn, J., Brandt, P., Schmidtko, S., & Krahmann, G. (2017). Decadal oxygen change in the eastern tropical North Atlantic. *Ocean Sci.*, *13*(4), 551–576. doi: 10.5194/os-13-551-2017

Hazeleger, W., & Drijfhout, S. (2006). Subtropical cells and meridional overturning circulation pathways in the tropical Atlantic. *J. Geophys. Res. Ocean.*, *111*(3), 1–13. doi: 10.1029/2005JC002942

Hsin, Y. C., & Qiu, B. (2012). Seasonal fluctuations of the surface North Equatorial Countercurrent (NECC) across the Pacific basin. *J. Geophys. Res. Ocean.*, *117*(6), 1–17. doi: 10.1029/2011JC007794

Hüttl-Kabus, S., & Böning, C. W. (2008). Pathways and variability of the off-equatorial undercurrents in the Atlantic Ocean. *J. Geophys. Res. Ocean.*, *113*(10), 1–14. doi: 10.1029/2007JC004700

Jochum, M., & Malanotte-Rizzoli, P. (2003). On the generation of North Brazil Current rings. *J. Mar. Res.*, *61*(2), 147–173. doi: 10.1357/002224003322005050

Jochum, M., & Malanotte-Rizzoli, P. (2004). A New Theory for the Generation of the Equatorial Subsurface Countercurrents. *J. Phys. Oceanogr.*, *34*(4), 755–771. doi: 10.1175/1520-0485(2004)034⟨0755:ANTFTG⟩2.0.CO;2

Kobayashi, S., Ota, Y., Harada, Y., Ebita, A., Ota, Y., Moriya, M., Onoda, H., Onogi, K., Kamahori, H., Kobayashi, C., Endo, H., Miyaoka, K., & Takahashi, K. (2015). The JRA-55 Reanalysis: General Specifications and Basic Characteristics. *J. Met. Soc. Jap.*, *93*(1), 5–48. doi: 10.2151/jmsj.2015-001

Large, W. G., & Yeager, S. (2004). Diurnal to decadal global forcing for ocean and sea-ice models: The data sets and flux climatologies. *NCAR Technical Note NCAR/TN-460+STR*. doi: 10.5065/D6KK98Q6

Marin, F., Hua, B. L., & Wacongne, S. (2000). The equatorial thermostad and subsurface countercurrents in the light of the dynamics of atmospheric Hadley cells. *J. Mar. Res.*, *58*(3), 405–437. doi: 10.1357/002224000321511098

McCreary Jr., J. P., Lu, P., & Yu, Z. (2002). Dynamics of the Pacific Subsurface Countercurrents. *J. Phys. Oceanogr.*, *32*, 2379–2404. doi: 10.1175/1520-0485(2002)032⟨2379:DOTPSC⟩2.0.CO;2

Oschlies, A., Brandt, P., Stramma, L., & Schmidtko, S. (2018). Drivers and mechanisms of ocean deoxygenation. *Nat. Geosci.*, *11*(7), 467–473. doi: 10.1038/s41561-018-0152-2

Schott, F. A., Dengler, M., Brandt, P., Affler, K., Fischer, J., Bourlès, B., … Rhein, M. (2003). The zonal currents and transports at 35W in the tropical Atlantic. *Geophys. Res. Lett.*, *30*(7), 35–38. doi: 10.1029/2002GL016849

Schott, F. A., McCreary Jr., J. P., & Johnson, G. C. (2004). Shallow Overturning Circulations of the Tropical-Subtropical Oceans. *Earth's Clim.*, *147*, 261–304.

Schott, F. A., Stramma, L., & Fischer, J. (1995). The warm water inflow into the western tropical Atlantic boundary regime , spring 1994. *J. Geophys. Res.*, *100*(C12), 24745 – 24760. doi: 10.1029/95JC02803

Stramma, L., Brandt, P., Schafstall, J., Schott, F., Fischer, J., & Körtzinger, A. (2008). Oxygen minimum zone in the North Atlantic south and east of the Cape Verde Islands. *J. Geophys. Res. Ocean.*, *113*(4), 1–15. doi: 10.1029/2007JC004369

Urbano, D. F., De Almeida, R. A., & Nobre, P. (2008). Equatorial Undercurrent and

North Equatorial Countercurrent at 38°W: A new perspective from direct velocity data. *J. Geophys. Res. Ocean.*, *113*(4), 1–16. doi: 10.1029/2007JC004215

Weisberg, R. H., & Weingartner, T. J. (1988). Instability Waves in the Equatorial Atlantic Ocean. *J. Phys. Oceanogr.*, *18*(11), 1641–1657. doi: 10.1175/1520-0485(1988)018⟨1641:IWITEA⟩2.0.CO;2

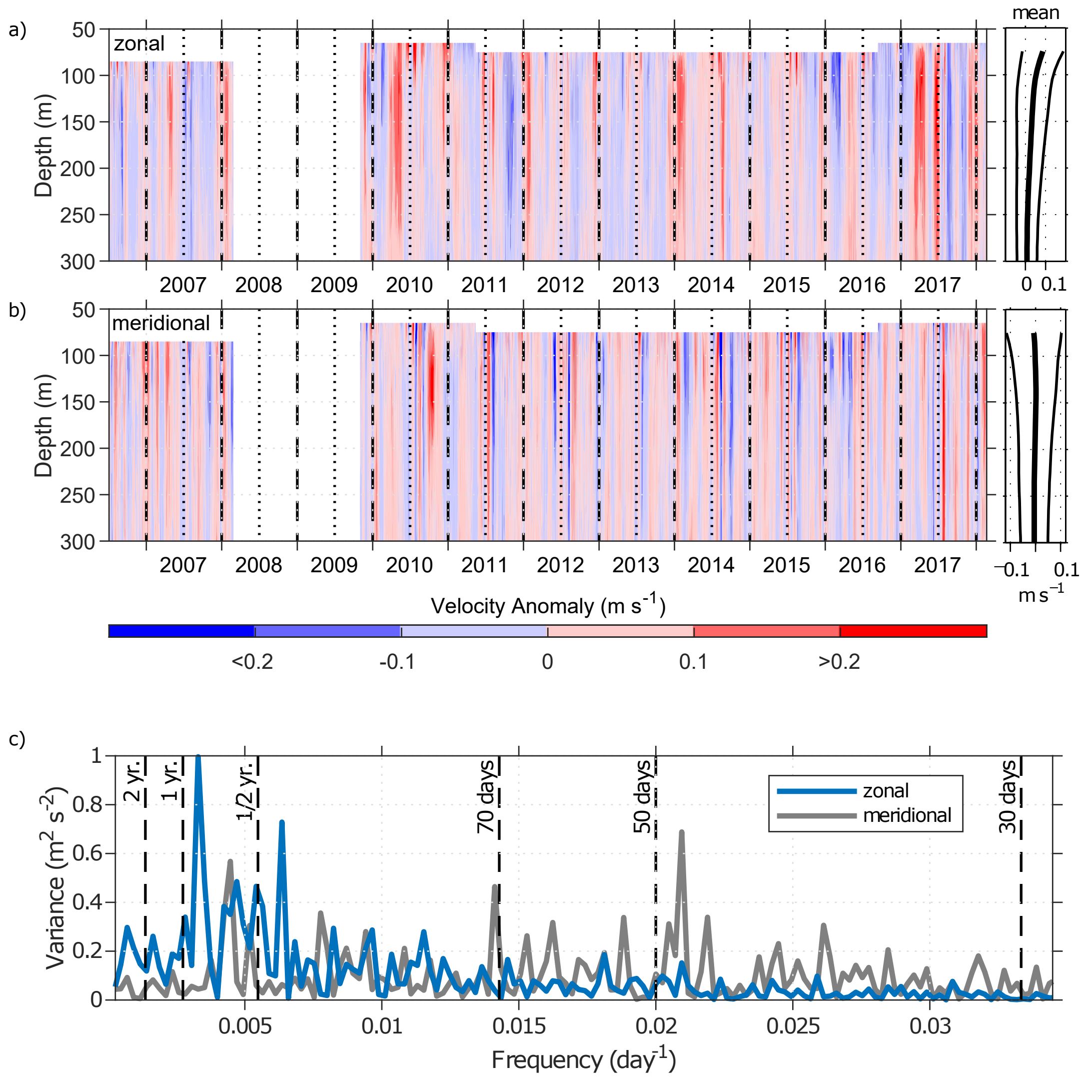

Figure 1. Anomalous (a) zonal and (b) meridional velocity measurements from moored ADCPs at 5°N, 23°W. The temporal mean profiles (thick black line) are shown at the right side of the (a) zonal and (b) meridional velocity time series. The thin black line marks the mean profile ± one standard deviation. (c) Lomb-Scargle periodogram of zonal (blue line) and meridional (grey line) velocity averaged between 95 m and 275 m depth.

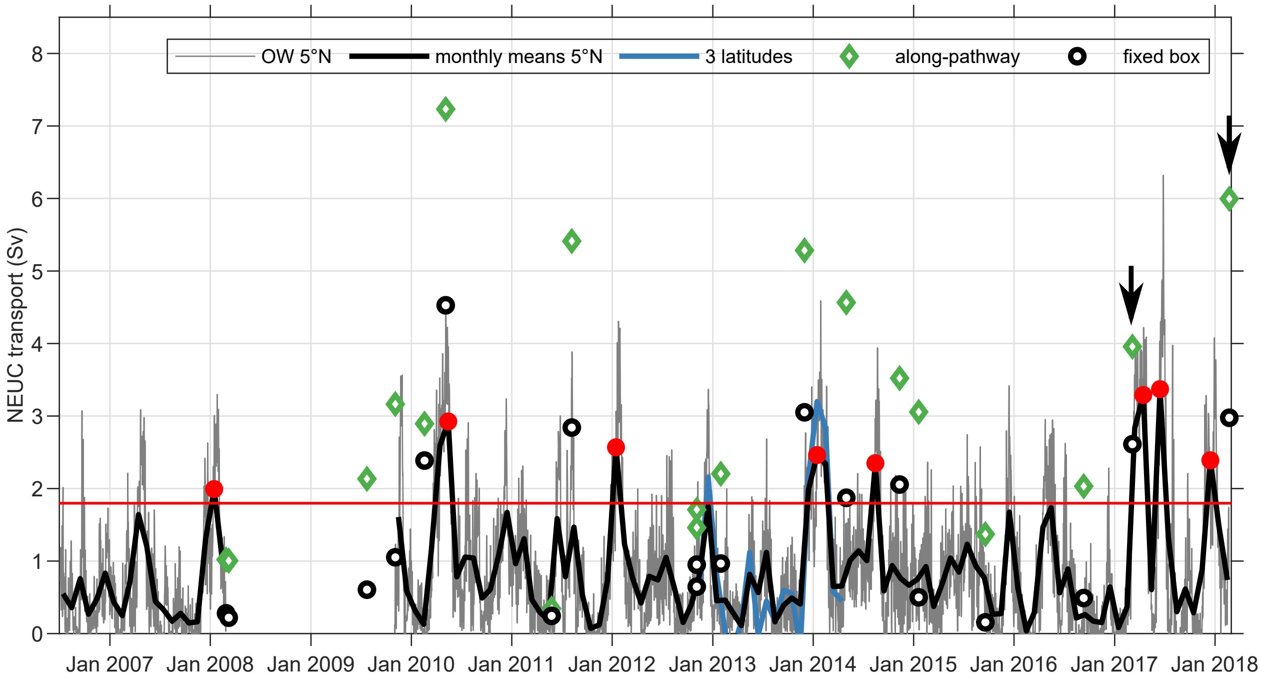

Figure 2. NEUC transport at 23°W calculated by four different methods: (i) from ship observations using a path following algorithm (green diamonds); (ii) from ship sections by integrating the eastward velocities in a fixed box (black circles); (iii) by the OW method combining ship sections and moored zonal velocities at three mooring positions (monthly means, blue line); (iv) by the OW method combining ship sections with moored zonal velocities at 5°N, 23°W (gray line). The black thick line shows the monthly mean values of the NEUC transport reconstructed at 5°N. The red line marks 2.5 times the standard deviation of the monthly mean transports used to define strong transport events (red dots). The black arrows mark the month of the cruises in 2017 and 2018.

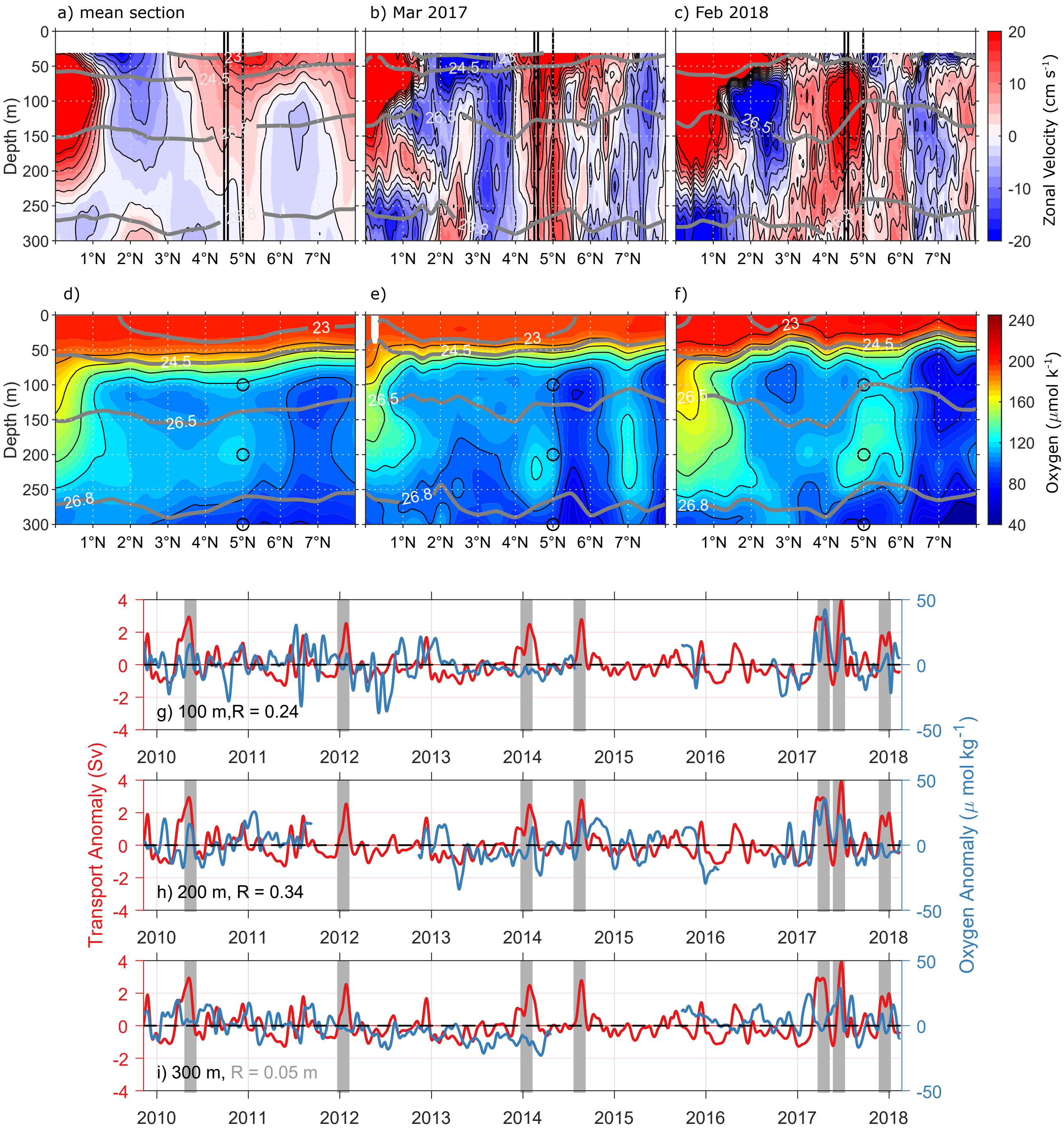

Figure 3. (a-f) Zonal velocity (a-c) and oxygen (d-f) observations along 23°W with mean sections of all 24 cruises (a,d) and sections taken during Ronald H. Brown cruise PNE 2017 (b,e) and during Meteor cruise M145 (c,f). Grey lines mark neutral density surfaces (kg m^{-3}), black vertical lines (a-c) mark the position of moorings, black circles (d-f) mark single point oxygen measurements. (g-i) 30-day low-pass filtered NEUC tranport (red lines) and oxygen anomalies (blue lines) at 5°N, 23°W at a depth of (g) 100 m, (h) 200 m, and (i) 300 m. Grey bars mark strong NEUC events. R is the correlation coefficient of zonal velocity and oxygen anomalies at zero lag (black/grey colour indicate that R is significant/not significant on a 95% confidence level).

Supporting Information for "Fluctuations of the Atlantic North Equatorial Undercurrent and associated changes in oxygen transports"

K. Burmeister[1], J. F. Lübbecke[2,3], P. Brandt[2,3], M. Claus[2,3], and J. Hahn[2]

[1]SAMS, Scottish Marine Institute, Oban, Argyll, PA37 1QA, United Kingdom

[2]GEOMAR Helmholtz Centre for Ocean Research Kiel, Düsternbrooker Weg 20, 24105 Kiel, Germany

[3]Christian-Albrechts-Universität zu Kiel, Christian-Albrechts-Platz 4, 24118 Kiel, Germany

Contents of this file

Text S1 to S3, Figures S1 to S7 and Table S1.

Introduction

In section S1 of the Supporting Information we give an detailed overview about the processing of the moored and shipboard observations. Section S2 presents details of the estimation of eastward transports from zonal velocity observations, their accuracies and uncertainties as well as their associated spatial patterns. In section S3 we investigate the relation between the NEUC transport and zonal wind stress in the tropical Atlantic.

S1: Moored and shipboard observations

Moored data

For our analysis we used velocity, hydrography and oxygen data from moorings at 5°N/23°W (Jul 2006-Feb 2008, Nov 2009-Jan 2018), 4.6°N/23.4°W (Nov 2012-Apr 2014) and 4.5°N/22.4°W (Nov 2012-Apr 2014). At all three mooring positions horizontal velocity was measured with downward (Jul 2006-Feb 2008) or upward (Nov 2009-Jan 2018) looking 75-kHz Longranger Acoustic Doppler Current Profilers (ADCPs). The ADCP configuration was set to a sampling period of 2 h, a bin length of 16 m and an ensemble number of 20 pings. A single velocity data point has a standard error of 1.7 $\mathrm{cm\,s^{-1}}$. Given the manufacturer's compass accuracy of 2°, we inferred a velocity error of < 4 % of the absolute measured velocity (Hahn et al., 2014). The minimum measurement range of all mooring periods is 85 m to 755 m. The moored velocity data was linearly interpolated onto a regular time-depth grid (12 h $\times$10 m), and a 40-h low-pass Butterworth filter was applied to remove the tidal signal from the time series (Fig. S1).

Eight pairs of oxygen (AADI Aanderaa optodes of model types 3830 and 4330) and Conductivity-Temperature-Depth (CTD) sensors (Sea-Bird SBE37 microcats) were installed at the moorings evenly distributed in the depth range from 100 m to 800 m. This configuration allows an appropriate estimate of the dissolved oxygen on density surfaces. All instruments were set to a sampling period of 2 h or shorter. The oxygen and CTD sensors were calibrated against CTD casts performed directly prior to or after the deployment period of the mooring. The oxygen sensors were additionally calibrated against laboratory measurements to expand the range of reference calibration points. For more details of the oxygen calibration see Hahn et al. (2014). The root mean square error of moored temperature, salinity and dissolved oxygen measurements was about 0.003°C, 0.006 and 3 μmol kg^{-1}, respectively (see Hahn et al., 2017). The point measured hydrography and oxygen data was interpolated onto a 12-h time grid.

Shipboard data

24 meridional velocity and 15 hydrographic and oxygen sections between 21°W and 26°W were obtained during cruises between 2002 to 2018 (Table S1). All ship sections cover at least the upper 350 m between 0° and 10°N. The velocity, hydrographic and oxygen ship sections used in this study are an extension of the data set used in Burmeister et al. (2019).

Velocity data were acquired by vessel-mounted ADCPs (vm-ADCPs). Vm-ADCPs continuously record velocities throughout a ship section and the accuracy of 1-h averaged data is better than 2-4 cm s^{-1} (Fischer et al., 2003). Hydrographic and oxygen data obtained during CTD casts were typically performed on a uniform latitude grid with half-degree resolution. The data accuracy for a single research cruise is generally assumed to be better than 0.002°C, 0.002 and 2 μmol kg^{-1} for temperature, salinity, and dissolved oxygen, respectively (Hahn et al., 2017). The single velocity, hydrographic and oxygen ship section were mapped on a regular grid (0.05° latitude $\times$ 10 m) and were smoothed by a Gaussian filter (horizontal and vertical influence (cutoff) radii: 0.05° (0.1°) latitude and 10 m (20 m), respectively). The single sections were averaged at each grid point to derive mean sections, which are again smoothed by the Gaussian filter. For the mean velocity, temperature, salinity and oxygen sections the standard error in the NEUC region

(65 – 270 m depth, 3° – 6.5°N) are 1.7 cm s^{-1}, 0.22°C, 0.02 and 3.8 μmol kg^{-1}, respectively.

S2: NEUC transport calculations

Path following algorithm

We derived estimates of the NEUC transport from the 24 meridional ship sections based on the algorithm of Hsin and Qiu (2012) which we consider as a reference NEUC transport. First, the central position Y_{CM} of the current is estimated using the concept of center of mass:

$$Y_{CM}(t) = \frac{\int_{Z_l}^{Z_u} \int_{Y_S}^{Y_N} y\ u(y,z,t)\ dy\ dz}{\int_{Z_l}^{Z_u} \int_{Y_S}^{Y_N} u(y,z,t)\ dy\ dz}, \tag{1}$$

where y is latitude, u is zonal velocity, z is depth, t is time, Z_u (Z_l) is upper (lower) boundary of the flow, and Y_N = 6°N (Y_S = 3.5°N) is the northern (southern) limit of the current core. We estimated a mean NEUC central position of 4.9°N and a standard deviation of ±0.3°.

Now the eastward velocity is integrated within a box whose meridional range is given by $Y_{CM}(t)$ and the southern (B_S) and northern (B_N) extent of the flow:

$$INT(t) = \int_{Z_l}^{Z_u} \int_{Y_{CM}-B_S}^{Y_{CM}+B_N} u(y,z,t)\ dy\ dz \tag{2}$$

For the integration we used the same boundary conditions as Burmeister et al. (2019). Z_u is the depth of the 24.5 kg m^{-3} and Z_l the depth of the 26.8 kg m^{-3} neutral density surface. The southern boundary is choosen as $Y_{CM} - 1.5°$ and the northern boundary is $Y_{CM} + 1.0°$. Note that, if no hydrographic measurements are available for a single ship section, the neutral density field derived from the mean hydrographic section is used.

Transport reconstruction

The eastward transport associated with the NEUC at about 23°W is computed using moored velocity data at 5°N, 23°W (2006-2018) as well as 4.6°N, 22.4°W (Nov. 2012-Apr. 2014) and 4.5°N, 23.4°W (Nov. 2012-Apr. 2014) combined with 24 meridional ship sections between 21°W and 26°W (Fig S1). In the main manuscript we reconstruct the NEUC transport using the optimal width (OW) method as described in Brandt et al. (2014). We chose this simple method because it is sufficient to represent the NEUC variability and more complex methods do not add any value, which we will show in this section. We validate the OW method using another approach from Brandt et al. (2014) based on Hilbert empirical orthogonal functions (HEOFs).

In the second approach the meridional sections of zonal velocity are reconstructed from the moored zonal velocities by interpolation and extrapolation using data taken at the mooring position. For the reconstruction of meridional sections we use variability patterns derived from the 24 meridional ship sections. Therefore we calculate HEOF pattern from the velocity sections between 4.25°N and 5.25°N, 65 m and 270 m (black dashed frame in Fig. S1). Here, a Hilbert transformation is applied to the zonal velocity fields before an EOF analysis is performed. The advantage of an HEOF is that the statistical patterns efficiently reveal spatial propagation features as for example a meridional migration of the current, in contrast to a traditional EOF. The first HEOF pattern explains 56% of variability contained in the ship section. The real pattern of the first HEOF shows a homogeneous change of velocities over the complete integration area (Fig. S3). Using only the first HEOF patterns to interpolate between the mooring positions by regressing the patterns onto the moored zonal velocity observations results in similar reconstructed transports as the OW method (black and red line in Fig. S4). As the homogeneous structure of the first HEOF explains most of the variability, there is no added value by including more HEOF patterns to reconstruct the NEUC transport. Nevertheless we want to mention here that the second pattern with a explained variance of 20% describes a meridional shift of the NEUC. A vertical shift of the NEUC might be described by the patterns of the third and fourth HEOF.

To investigate whether the dominant pattern of the first HEOF of the zonal velocities between 4.25°N and 5.25°N represents a meridional migration of the NEUC out of the calculation area the HEOF method is repeated using the zonal velocities between 3.5°N and 6.0°N. This region covers the southern and northern boundary of the NEUC even if the current is meridionally migrating. The fixed box integrated transports for this region calculated from the ship sections (gray squares in Fig. S4) agrees well with the reference transports. Again, the real pattern of the first HEOF shows a homogeneous change of zonal velocity although it explains less variability compared to the first HEOF of the smaller box. Furthermore, the first and second pattern which explain together 66% of the velocity variability seem to describe a meridional shift of the current. Nevertheless, the eastward transport time series reconstructed using the first (yellow line in Fig. S4) or the first two HEOF pattern (blue line in Fig. S4) of zonal velocities between 3.5°N and 6.0°N agrees well with that reconstructed from velocities between 4.25°N and 5.25°N. The mean transport estimates using the bigger box is 1.9 Sv.

In summary, the reconstructed eastward transports between 4.25°N and 5.25°N tend to underestimate the mean current strength of the NEUC, however the time series is able to capture the NEUC variability reasonably well. We choose the smaller box to reconstruct the NEUC transport variability due to the smaller uncertainty of the reconstructed transports when using only the mooring at 5°N, 23°W.

S3: NEUC and sea surface winds

Auxiliary data

Monthly mean JRA-55 surface wind velocities (U_h, Kobayashi et al., 2015) on a 1.25°×1.25° horizontal grid for the time period from 2006 to 2018 are used in this study. We calculated the wind stress τ_h from the JRA-55 reanalysis data using the Bulk formula $\tau_h = \rho_{air} C_D |U_h| U_h$, where $\rho_{air} = 1.22\mathrm{kg\,m^{-3}}$ is the density of air, $C_D = 0.0013$ is the wind drag coefficient and $|U_h|$ is the absolute value of U_h.

Furthermore, we are using monthly mean wind stress from the ASCAT on METOP Level 4 Daily Gridded Mean Wind Fields (Bentamy & Fillon, 2012). The dataset has a horizontal resolution of 0.25° covering the time period from April 2007 to May 2018. For comparison, ASCAT wind stress data are regridded onto the horizontal grid of the JRA-55 reanalysis data (1.25°) by bin averaging.

Linear regression

We performed a lead-lag regression of zonal wind stress anomalies with respect to the 2008 to 2017 climatology onto the reconstructed NEUC time series for two different wind products (Fig. S6). The regression pattern of both wind products generally agree. Differences in the wind stress products may arise from the different kind of data that is used. Another source of uncertainty may be different Bulk formulas used for the wind stress calculations, which can result in an uncertainty up to 20% (Large & Yeager, 2004).

In the linear regression patterns, easterly wind stress anomalies between 12°S and 6°N east of about 25°W are leading the NEUC transports by one to two months. Along the equator, these easterly wind stress anomalies may trigger equatorial Kelvin waves. These Kelvin waves may remotely generate Rossby waves traveling as far as 5°N, 23°W by reflecting at the eastern boundary into Rossby waves and coastal trapped waves traveling northward along the coast and generating Rossby waves when the topography is turning north. Rossby waves at 5°N, 23°W may also be generated locally (Burmeister et al., 2016; Foltz et al., 2010). In the ASCAT and JRA-55 data easterly wind stress anomalies above the NEUC region with decreasing magnitude towards the north lead the NEUC transports by two months. The decreasing zonal wind stress indicates changes in the wind stress curl, which may locally generate Rossby waves altering the NEUC flow. Furthermore local zonal wind stress anomalies along the northern coastline of the Gulf of Guinea can trigger westward propagating coastal trapped waves which again generate Rossby waves radiating from the coast when the topography turns north (Chu et al., 2007). In general, the relative low coefficient of correlation ($R<0.45$) suggest that the wind stress field can only explain some part of the NEUC variability and other processes must contribute.

References

Bentamy, A., & Fillon, D. C. (2012). Gridded surface wind fields from Metop/ASCAT measurements. *Int. J. Remote Sens.*, *33*(6), 1729–1754. doi: 10.1080/01431161.2011.600348

Brandt, P., Funk, A., Tantet, A., Johns, W. E., & Fischer, J. (2014). The Equatorial Undercurrent in the central Atlantic and its relation to tropical Atlantic variability. *Clim. Dyn.*, *43*(11), 2985–2997. doi: 10.1007/s00382-014-2061-4

Burmeister, K., Lübbecke, J. F., & Brandt, P. (2016). Revisiting the cause of the eastern equatorial Atlantic cold event in 2009. *J. Geophys. Res. Ocean.*, *7*(121), 4777–4789. doi: 10.1002/2016JC011719

Burmeister, K., Lübbecke, J. F., Brandt, P., & Duteil, O. (2019). Variability of the Atlantic North Equatorial Undercurrent and its impact on oxygen. *J. Geophys. Res. Ocean.*, *in review*(X), X.

Chu, P. C., Ivanov, L. M., Melnichenko, O. V., & Wells, N. C. (2007). On long baroclinic Rossby waves in the tropical North Atlantic observed from profiling floats. *J. Geophys. Res.*, *112*(C5), C05032. doi: 10.1029/2006JC003698

Fischer, J., Brandt, P., Dengler, M., Müller, M., & Symonds, D. (2003). Surveying the upper ocean with the ocean surveyor: A new phased array Doppler current profiler. *J. Atmos. Ocean. Technol.*, *20*(5), 742–751. doi: 10.1175/1520-0426(2003)20⟨742:STUOWT⟩2.0.CO;2

Foltz, G. R., & McPhaden, M. J. (2010). Interaction between the Atlantic meridional and Niño modes. *J. Geophys. Res.*, *37*(18), L18604. doi: 10.1029/2010GL044001

Hahn, J., Brandt, P., Greatbatch, R. J., Krahmann, G., & Körtzinger, A. (2014). Oxygen variance and meridional oxygen supply in the Tropical North East Atlantic oxygen minimum zone. *Clim. Dyn.*, *43*(11), 2999–3024. doi: 10.1007/s00382-014-2065-0

Hahn, J., Brandt, P., Schmidtko, S., & Krahmann, G. (2017). Decadal oxygen change in the eastern tropical North Atlantic. *Ocean Sci.*, *13*(4), 551–576. doi: 10.5194/

os-13-551-2017

Hsin, Y. C., & Qiu, B. (2012). Seasonal fluctuations of the surface North Equatorial Countercurrent (NECC) across the Pacific basin. *J. Geophys. Res. Ocean.*, *117*(6), 1–17. doi: 10.1029/2011JC007794

Jochum, M., & Malanotte-Rizzoli, P. (2004). A New Theory for the Generation of the Equatorial Subsurface Countercurrents. *J. Phys. Oceanogr.*, *34*(4), 755–771. doi: 10.1175/1520-0485(2004)034⟨0755:ANTFTG⟩2.0.CO;2

Kobayashi, S., Ota, Y., Harada, Y., Ebita, A., Ota, Y., Moriya, M., Onoda, H., Onogi, K., Kamahori, H., Kobayashi, C., Endo, H., Miyaoka, K., & Takahashi, K. (2015). The JRA-55 Reanalysis: General Specifications and Basic Characteristics. *J. Met. Soc. Jap.*, *93*(1), 5–48. doi: 10.2151/jmsj.2015-001

Large, W. G., & Yeager, S. (2004). Diurnal to decadal global forcing for ocean and sea-ice models: The data sets and flux climatologies. *NCAR Technical Note NCAR/TN-460+STR*. doi: 10.5065/D6KK98Q6

Table S1. Meridional ship sections taken between 21°W and 26°W from 2002 to 2018. All sections cover at least the upper 350 m from 0°N to 10°N. For all sections ADCP data is available. Sections including oxygen (O_2) and hydrography (CTD) measurements are marked accordingly.

cruise	date	averaged longitude	latitude	O_2/CTD
Meteor 55	Oct-Nov 2002	24°W	0°-10°N	no
Ronald H. Brown A16N	Jun-Aug 2003	26°W	6°S-10°N	no
Ronald H. Brown PNE6	Jun 2006	23°W	5°S-13.5°N	yes
Ronald H. Brown PNE6	Jun-Jul 2006	23°W	5°S-14°N	yes
Meteor 68/2	Jun-Jul 2006	23°W	4°S-14°N	yes
L'Atalante IFM-GEOMAR 4	Feb 2008	23°W	2°S-14°N	yes
L'Atalante IFM-GEOMAR 4	Mar 2008	23°W	2°S-14°N	no
Ronald H. Brown PNE09	Jul-Aug 2009	23°W	0°-14°N	no
Meteor 80/1	Oct-Nov 2009	23°W	6°S-14°N	yes
Meteor 81/1	Feb-Mar 2010	21°W	6°S-13°N	no
Ronald H. Brown PNE10	May 2010	23°W	0°-14°N	yes
Maria S. Merian 18/2	May-Jun 2011	23°W	0°-14°N	no
Ronald H. Brown PNE11	Jul-Aug 2011	23°W	0°-14°N	no
Maria S. Merian 22	Oct-Nov 2012	23°W	6°S-8°N	yes
Maria S. Merian 22	Oct-Nov 2012	23°W	0°-14°N	no
Ronald H. Brown PNE13a	Jan-Feb 2013	23°W	0°-14°N	no
Ronald H. Brown PNE13b	Nov-Dec 2013	23°W	6°S-14°N	yes
Meteor 106	Apr-May 2014	23°W	6°S-14°N	yes
Polarstern PS88.2	Oct-Nov 2014	23°W	2°S-14°N	yes
Endeavor EN-550	Jan 2015	23°W	2°S-14°N	yes
Meteor 119	Sep-Oct 2015	23°W	5.5°S-14°N	yes
Meteor 130	Aug-Oct 2016	23°W	6°S-14°N	yes
Ronald H. Brown PNE17	Feb-Mar 2017	23°W	4°S-14°N	yes
Meteor 145	Feb-Mar 2018	23°W	6°S-14°N	yes

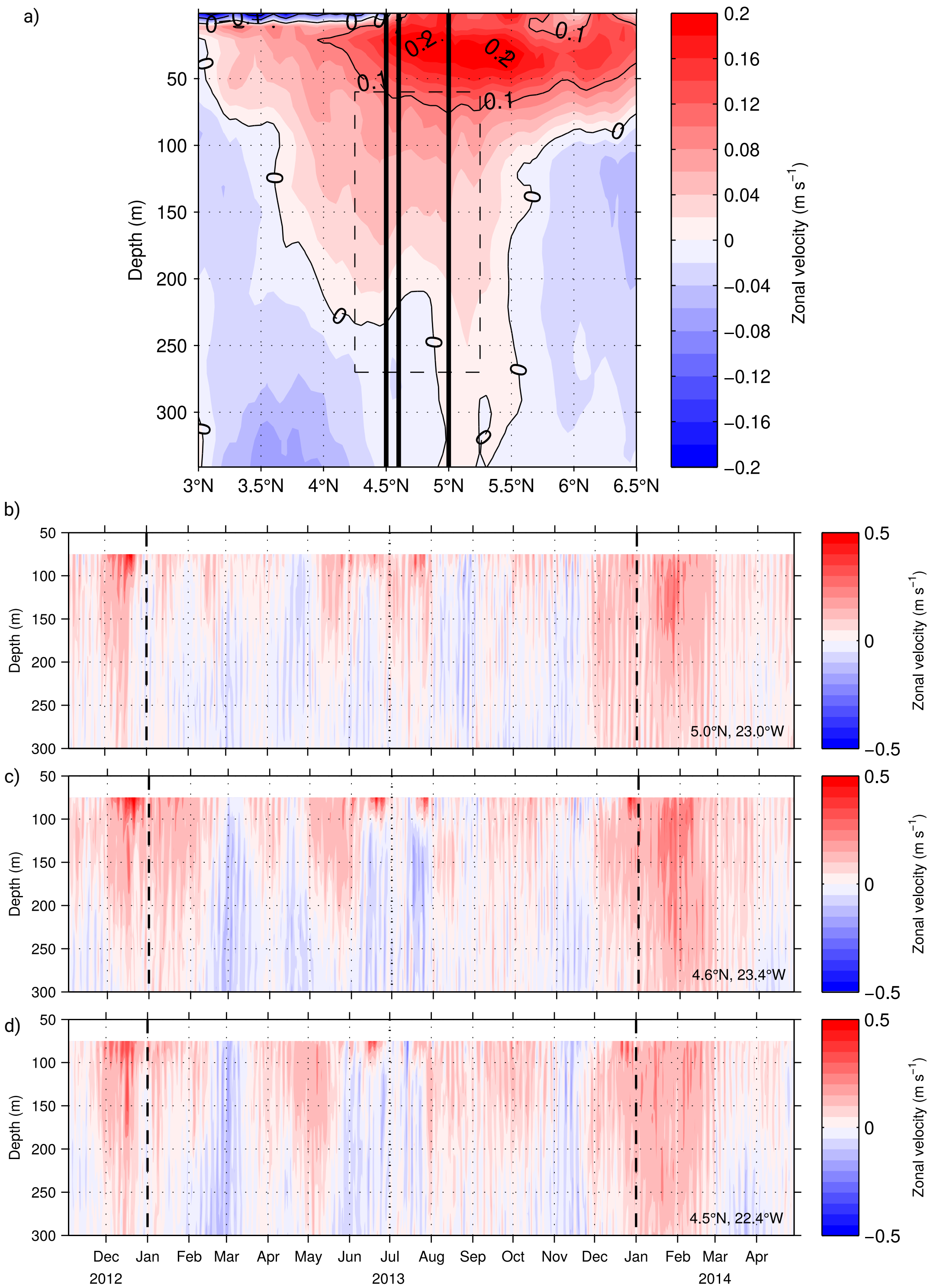

Figure S1. (a) Mean zonal velocity along 23°W estimated on the basis of 24 ship sections taken during 2002 and 2018. Black vertical lines mark the latitudinal position of the three moorings. The black dashed frame marks the box for the transport reconstruction. (b,c,d) Zonal velocity observations at the mooring positions (b) 5.0°N, 23°W, (c) 4.6°N, 23.4°W and (d) 4.5°N, 22.4°W.

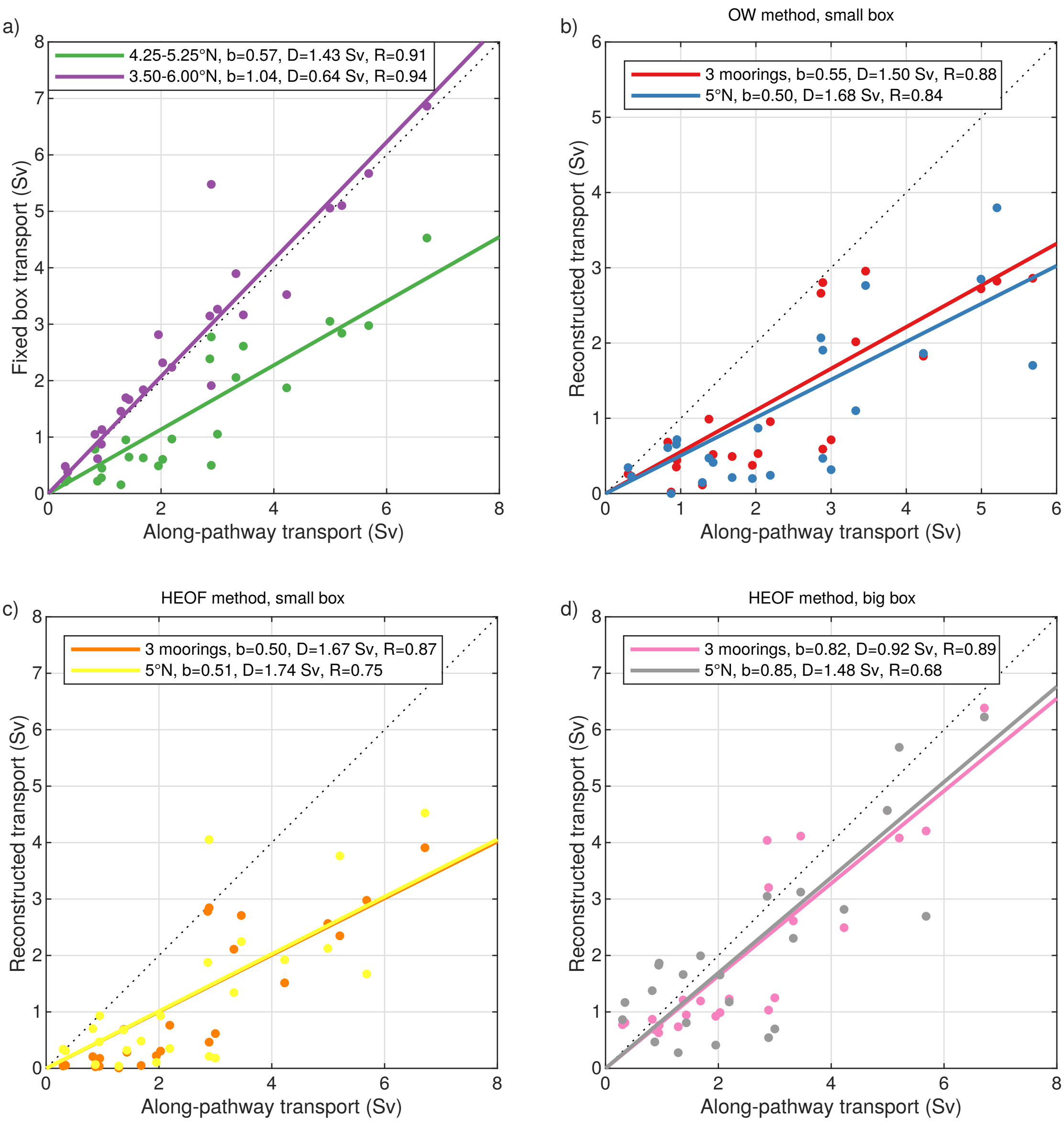

Figure S2. Regression slope b, mean difference D and correlation coefficient R between the reference NEUC transport (along-pathway transport) and the reconstructed transports based on different methods: (a) fixed box integrated transports between 4.25°N and 5.25°N (green) as well as between 3.50°N and 6.00°N (purple), (b) OW method using 3 moorings (red) and only the 5°N mooring, (c) HEOF method using the first HEOF pattern applied to 3 moorings (orange) and only to the 5°N mooring (yellow) for the area between 4.25°N and 5.25°N, (d) HEOF method using the first HEOF pattern applied to 3 moorings (pink) and only to the 5°N mooring (grey) for the area between 3.50°N and 6.00°N.

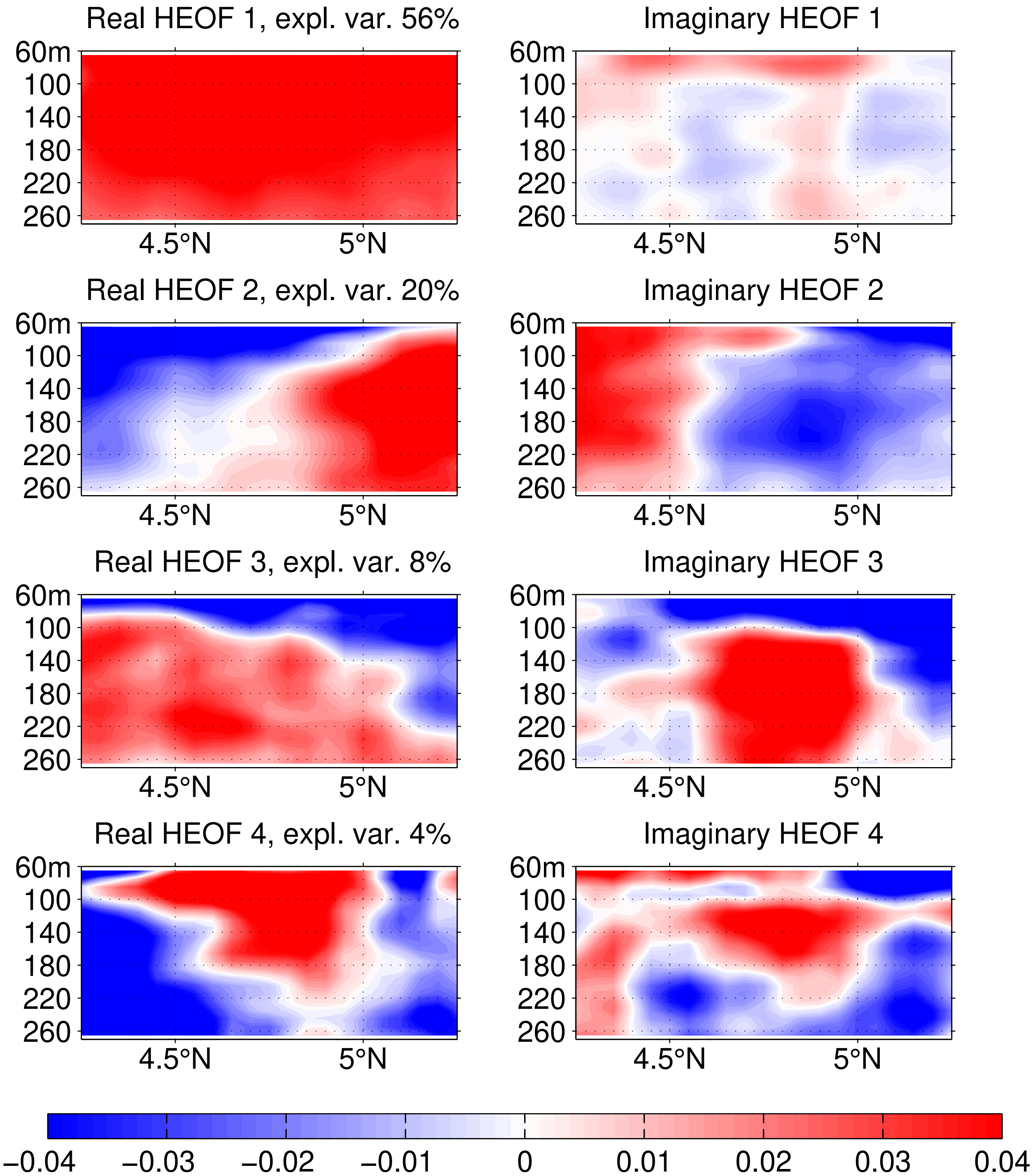

Figure S3. Real (left panels) and imaginary (right panels) dimensionless pattern of the first four Hilbert empirical orthogonal functions calculated from the 24 zonal velocity sections along 23°W between 4.25°N and 5.25°N, 65 m and 270 m depth.

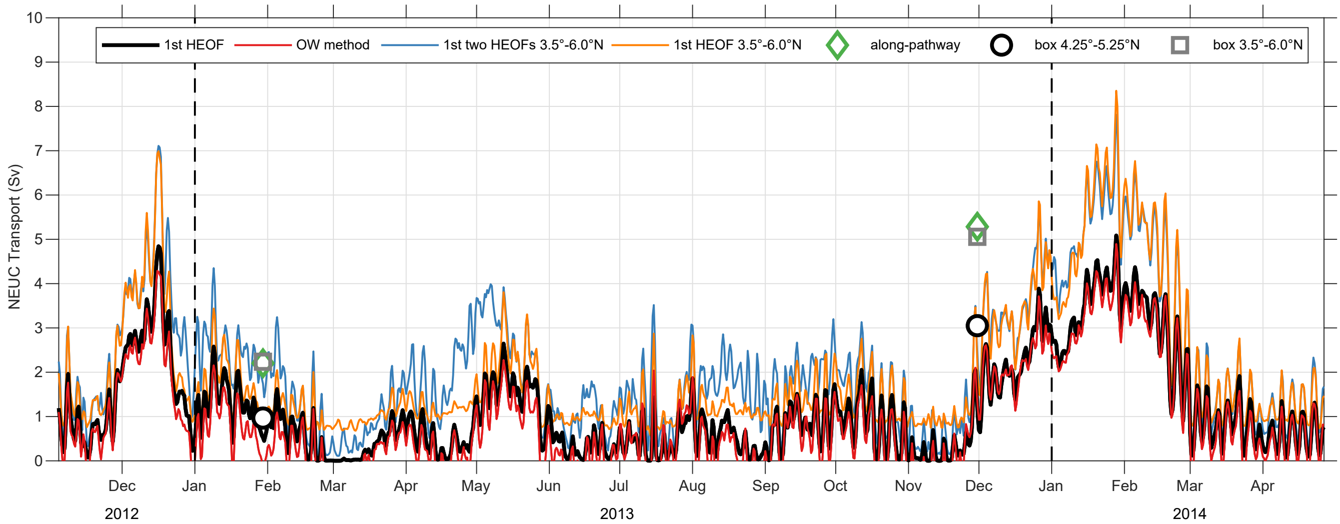

Figure S4. NEUC transport at 23°W calculated by different methods: (i) from ship observations using a path following algorithm (green diamonds); (ii) from ship sections by integrating the eastward velocities in a fixed box between 4.25°N and 5.25°N (black circles) and 3.5°N and 6.0°N (grey squares); (iii) by the HEOF method combining ship sections and moored zonal velocities at three mooring positions using the first HEOF of velocities between 4.25°N and 5.25°N (black line) as well as using the first (orange line) or the first two (blue line) HEOF of velocities between 3.5°N and 6.0°N; (iv) by the OW method combining ship sections between 4.25°N and 5.25°N and moored zonal velocities at three mooring positions (red line).

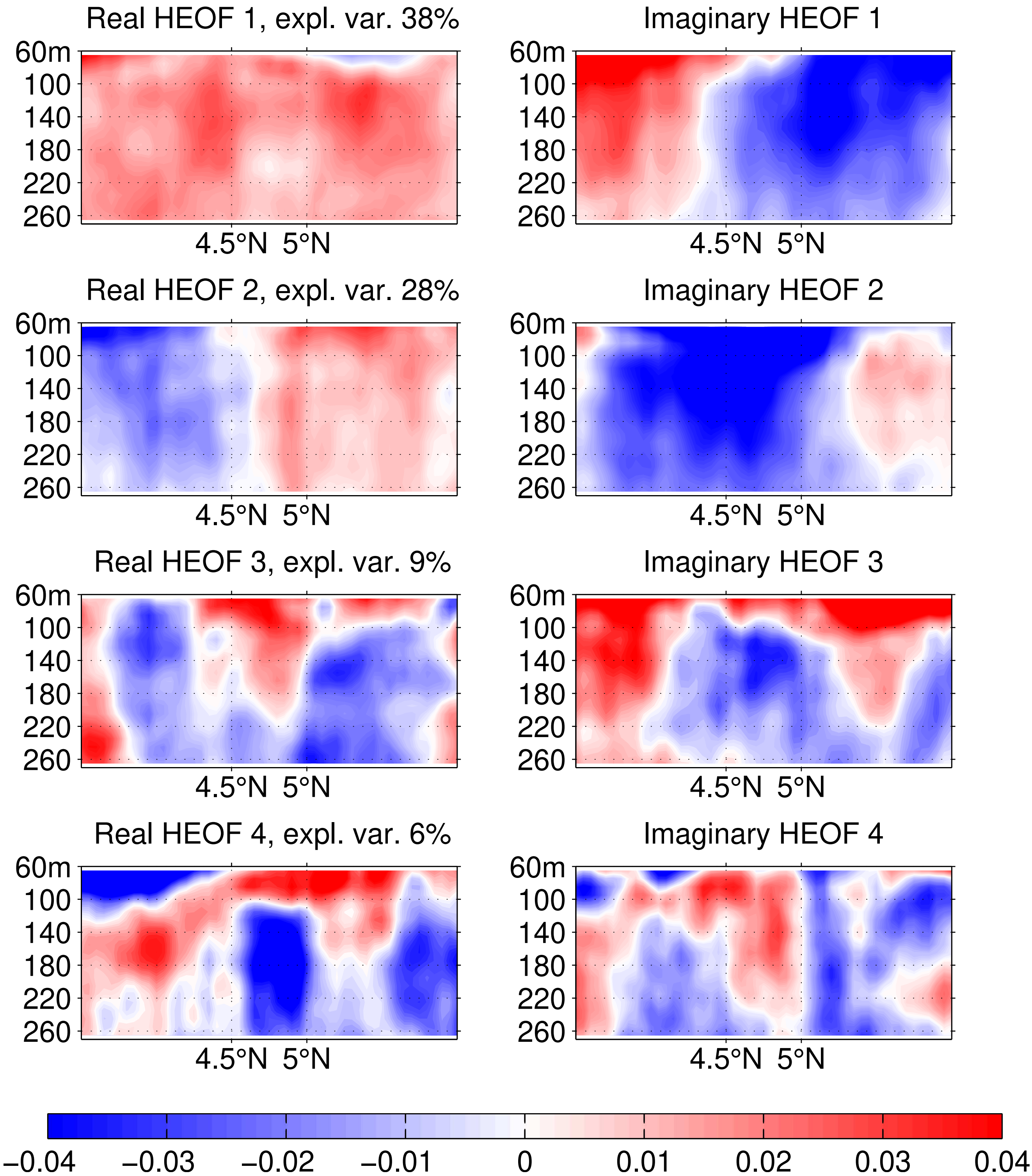

Figure S5. Real (left panels) and imaginary (right panels) dimensionless pattern of the first four Hilbert empirical orthogonal functions calculated from the 24 zonal velocity sections along 23°W between 3.5°N and 6.0°N, 65 m and 270 m depth.

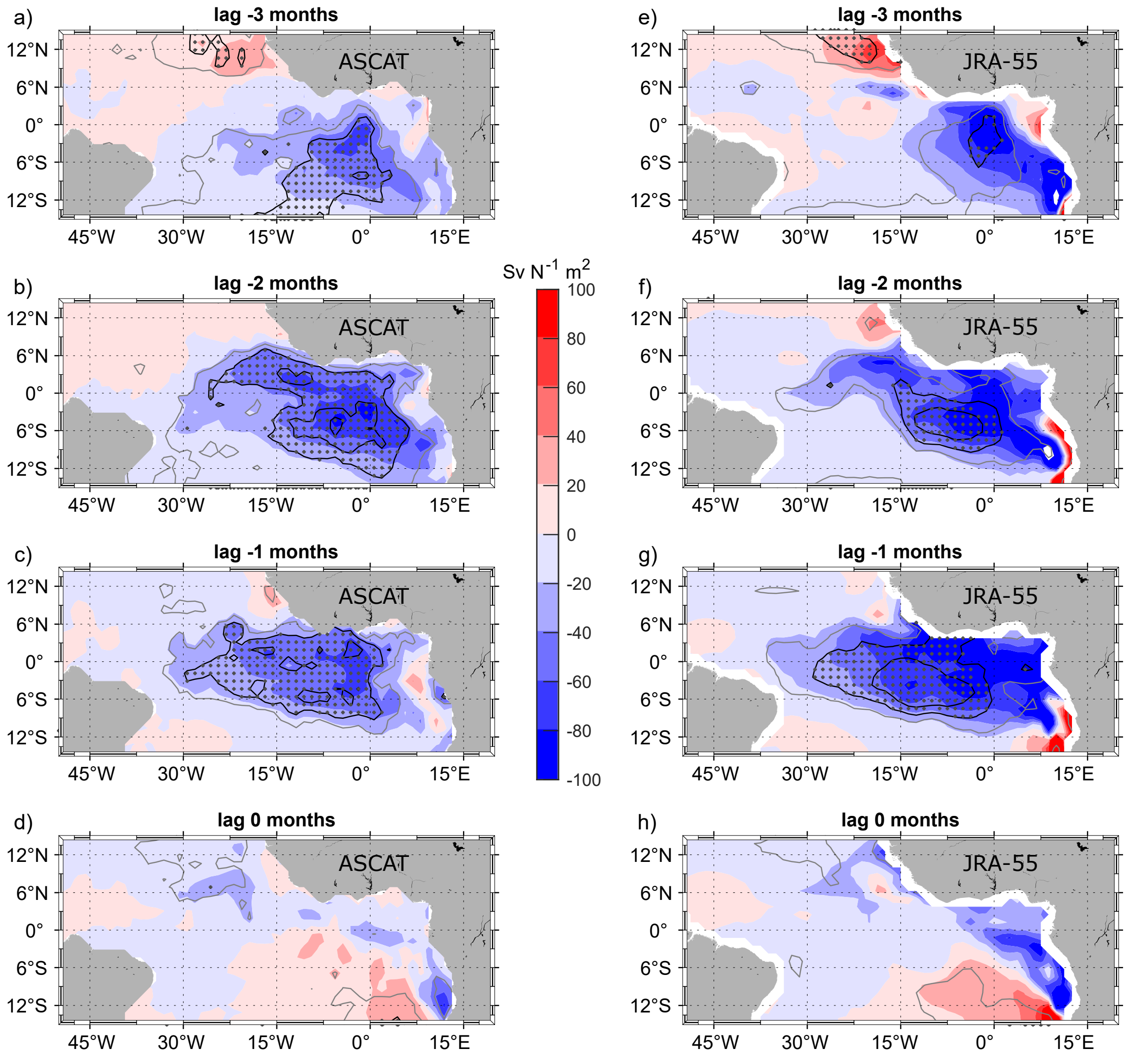

Figure S6. Slope of lead-lag regression of monthly mean zonal wind stress anomalies with respect to the 2008-2017 climatology onto the reconstructed monthly mean NEUC transport time series. Results are shown for ASCAT (a-d) and JRA-55 reanalysis (e-h). Contour lines show the coefficient of correlation (R) with an interval of 0.1, the grey contour marks R=0.1. Grey crosses mark significant values of R.

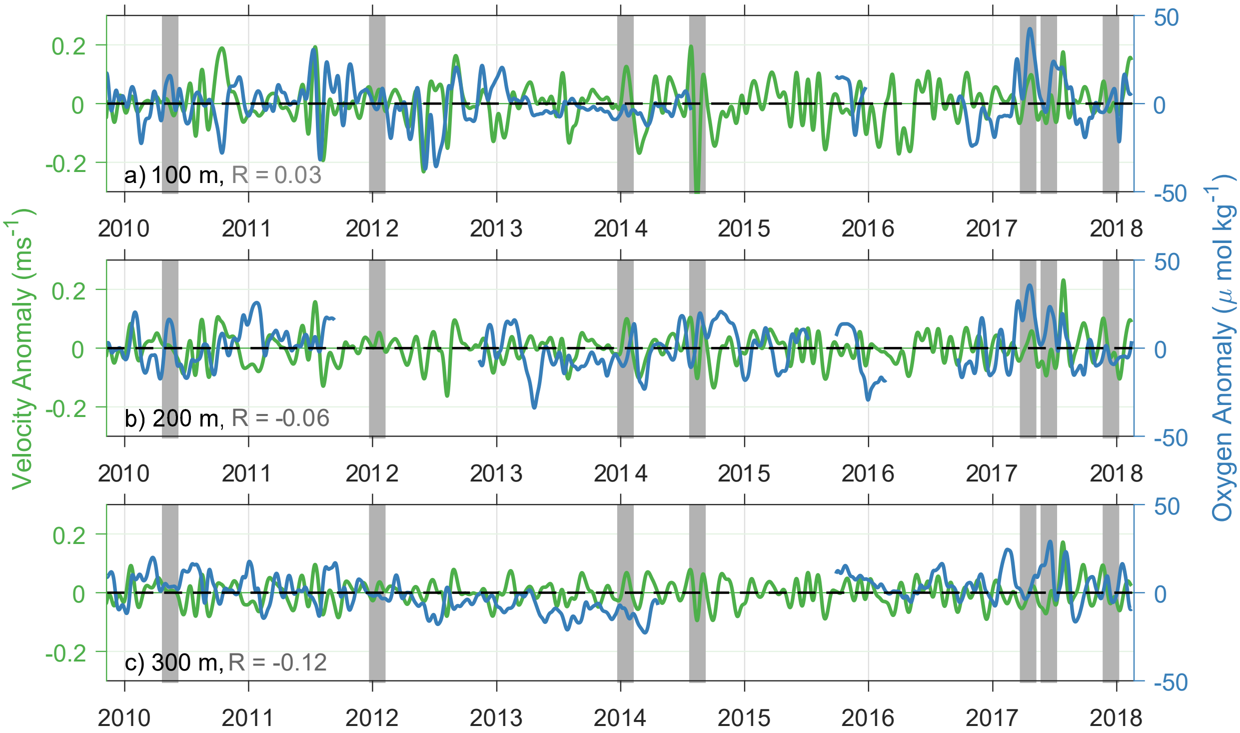

Figure S7. 30-day low-pass filtered (a-c) meridional velocity anomalies (green lines) and oxygen anomalies (blue lines) at 5°N, 23°W at a depth of (a) 100 m, (b) 200 m, and (c) 300 m. Grey bars mark strong NEUC events. The correlation coefficient R at zero lag is not significant on a 95% confident interval.